

# Self-Induced Superradiant Masing

Wenzel Kersten,<sup>1,\*</sup> Nikolaus de Zordo,<sup>1</sup> Elena S. Redchenko,<sup>1</sup> Nikolaos Lagos,<sup>1</sup> Andrew N. Kanagin,<sup>1</sup>  
Andreas Angerer,<sup>1</sup> William J. Munro,<sup>2</sup> Kae Nemoto,<sup>2</sup> Igor E. Mazets,<sup>1</sup> and Jörg Schmiedmayer<sup>1,†</sup>

<sup>1</sup>Vienna Center for Quantum Science and Technology, Atominstitut, TU Wien, Stadionallee 2, A-1020 Vienna, Austria

<sup>2</sup>Okinawa Institute of Science and Technology Graduate University,  
1919-1 Tancha, Onna-son, Kunigami-gun, Okinawa 904-0495, Japan

(Dated: February 14, 2024)

We study superradiant masing in a hybrid system composed of nitrogen-vacancy center spins in diamond coupled to a superconducting microwave cavity. After the first fast superradiant decay we observe transient pulsed and then quasi-continuous masing. This emission dynamics can be described by a phenomenological model incorporating the transfer of inverted spin excitations into the superradiant window of spins resonant with the cavity. After experimentally excluding cQED effects associated with the pumping of the masing transition we conjecture that direct higher-order spin-spin interactions are responsible for creating the dynamics and the transition to the sustained masing. Our experiment thus opens up a novel way to explore many-body physics in disordered systems through cQED and superradiance.

In cavity quantum electrodynamics (cQED) [1] and particularly superradiance [2, 3], the emitters are generally assumed to be independent and non-interacting [4]. Interactions only come about through the emitted light itself [5]. These mediated interactions lead to an extremely rich zoo of phases and phase transitions in the emitter-light system [6–9]. The role of genuine many-body physics coming from direct interactions between the emitters in these systems, however, remains elusive.

Superradiance – enhanced collective emission exhibiting high coherence and a nonlinear scaling of the intensity with the number of emitters [4] – has been observed in many systems [10–14] including solid-state realizations with quantum dots [15, 16] and the negatively charged nitrogen-vacancy centers (NV<sup>-</sup>) in diamond [17, 18]. In this solid-state context where billions of emitters are confined on a  $\mu\text{m}$  scale, the direct dipole-dipole interactions start to play a larger role.

In our experiment, we investigate a dense ensemble of NV<sup>-</sup> spins strongly and homogeneously coupled to a MW cavity which can be tuned in and out of resonance much faster than the timescales of the spin ensemble. The setup details are outlined in Ref. [19], where we demonstrated the triggered superradiant emission from an inverted spin ensemble. Our system, illustrated in Fig. 1a, allows for the application of strong microwave inversion pulses and readout using a heterodyne detection scheme. The cavity is made of two parallel sapphire chips, each featuring a superconducting split-ring structure. The diamond sample, a cube with side length of around 200  $\mu\text{m}$ , is positioned between the chips. A detuning loop is wrapped directly around the chips and used for rapid switching of the external magnetic field. This assembly is then placed in a copper box and located inside a dilution refrigerator operating at 25 mK. The cavity has a resonance frequency of around  $\omega_c/2\pi = 3.1$  GHz and linewidth  $\kappa/2\pi = 418$  kHz (half-width at half-maximum). The  $N \approx 5.3 \times 10^{12}$  NV<sup>-</sup> spins are coupled to the cavity

with a collective coupling strength of  $g_{\text{coll}}/2\pi = 4.6$  MHz, where the single spin coupling of  $g_0/2\pi \approx 2$  Hz is uniform over the sample volume – a necessary requirement for the superradiant dynamics we observe. The spin system has an effective ensemble linewidth of  $\Gamma/2\pi = 3.6$  MHz due to the inhomogeneously broadened spin frequency distribution  $\rho(\omega)$  [20], with a width of  $W/2\pi = 9.2$  MHz (full-width at half-maximum), and individual spin linewidths of  $\gamma_{\perp}/2\pi \approx 0.2$  MHz. Next, the typical nearest-neighbor distance between NV<sup>-</sup> spins in our diamond sample with roughly 6 ppm concentration is  $r \approx 10$  nm. That results in a spin-spin coupling strength between neighboring NV<sup>-</sup>s of  $J_n/2\pi \approx 52$  kHz. Further details are provided in the Supplementary Methods section and in Supplementary Fig. 1.

## Initial superradiant decay

For all experiments, we employ the previously established protocol [19] for generating a uniformly inverted spin state. All NV<sup>-</sup> spins are tuned into resonance with the cavity, using a static magnetic field with equal projections along the four diamond axes. We apply a microwave inversion pulse to homogeneously invert all spins from a relaxed initial state of the effective two-level systems. Subsequently, the spin ensemble is rapidly detuned from the cavity resonance and stored for a set hold time. This procedure allows for the preparation of states with uniform initial spin inversion  $p_0 = \langle \sigma_z^i \rangle$  and almost zero transversal spin components  $\langle \sigma_{\pm}^i \rangle \approx 0$ . The values for  $p_0$ , bounded by  $\pm 1$ , are tunable within the range of 0.1 to 0.4 by modifying the hold time on the order of milliseconds.

Upon tuning the spins back into resonance with the cavity using the detuning loop, the inverted spin state is free to interact with the cavity mode. If the stored inversion is above the threshold given by  $p_0 C > 1$  [20], where  $C = g_{\text{coll}}^2/\kappa\Gamma \approx 14$  is the cooperativity of the coupled system, it enters a metastable state. In this state, any fluctuation will stimulate a collective emission pro-

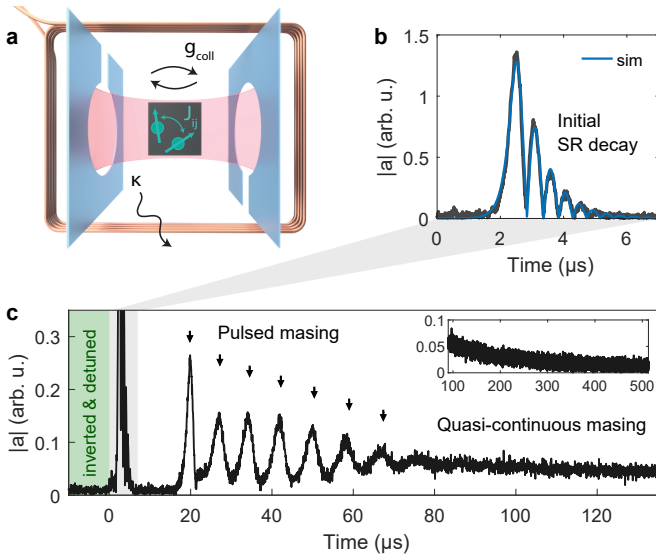


**FIG. 1. Experimental setup and superradiant masing dynamics.** **a**, Schematic of the superconducting microwave cavity strongly coupled to the  $NV^-$  diamond. The cavity is made of two parallel chips with split-ring structures inside a copper box. A superconducting wire loop surrounding the chips facilitates rapid spin detuning. **b**, Zoomed-in plot of the cavity amplitude  $|a|$  during the initial superradiant (SR) decay, which is triggered upon tuning the inverted spin ensemble back into resonance and is well described by a semi-classical model. **c**, After the initial superradiant decay we observe a series of narrow masing pulses evolving into a quasi-continuous cavity emission, slowly decreasing over a long timescale of half a millisecond (see inset). Note the different y-axis scaling in **b** and **c**.

cess known as a superradiant decay [21]. Conversely, if the inversion is below the instability threshold, dephasing due to inhomogeneous broadening becomes dominant and prevents the avalanche process. In our case, the superradiant decay is triggered by noise photons from the input line. As the spin decay accelerates, the cavity amplitude  $|a|$  increases. It reaches its maximum when the collective spin vector points towards the equator of the Bloch sphere. Subsequently, the energy is coherently exchanged between cavity and spins, visible as damped Rabi oscillations in Fig. 1b. This coherent exchange is eventually stopped due to loss processes in the system, with the main contribution being the dephasing of the inhomogeneously broadened spins. The superradiant decay dynamics is well-captured by the Maxwell-Bloch equations [22], a standard semi-classical description involving non-interacting spins coupled to the cavity.

### Pulsed revivals and quasi-continuous masing

Surprisingly, following a pause of  $\Delta t \approx 15 \mu s$  after the initial superradiant decay, a sequence of revival pulses emerges, as shown in Fig. 1c, which goes beyond the standard description. The revival dynamics timescale is unexpected, as it is much longer than the characteristic

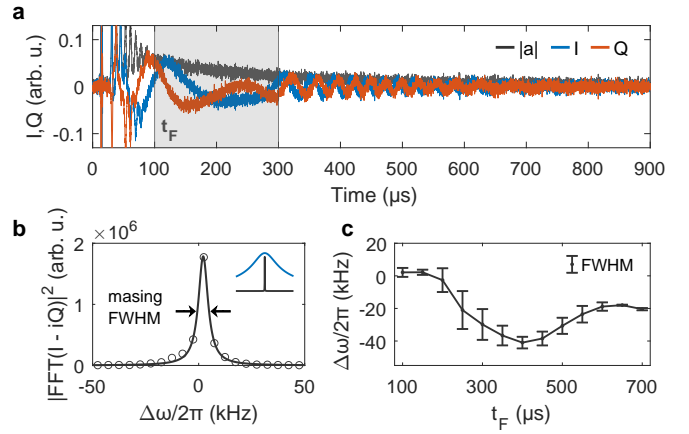


**FIG. 2. Spectral analysis of quasi-continuous masing emission.** **a**, Long tail of the quasi-continuous masing emission, showing the quadratures  $I$  and  $Q$  of the cavity amplitude  $|a|$ , digitally demodulated in the rotating frame of the cavity resonance frequency for visual clarity. The gray shaded area marks the interval for the Fourier analysis, which is plotted in **b**, where the emission has a linewidth much smaller than the cavity, see inset. The frequency difference  $\Delta\omega/2\pi$  is relative to the cavity frequency of 3.1 GHz. **c**, The frequency and linewidth of the emission changes over time when the window of the Fourier analysis is shifted.

timescales of the cavity loss rate, the ensemble dephasing, and the collective interaction of the coupled system,  $\Delta t \gg \{\kappa, \Gamma, g_{\text{coll}}\}^{-1}$ . It also significantly exceeds the individual spin linewidth  $\Delta t \gg \gamma_{\perp}^{-1}$ . This excludes any Rabi oscillations or spin-echo behavior as a possible explanation for the revivals. The revival pulses manifest as distinct peaks in the cavity amplitude, progressively spreading over time. These masing pulses are approximately Gaussian, featuring full-widths at half-maximum ranging from around  $1.2 \mu s$  to  $2.9 \mu s$ . Each pulse has a random but nearly constant phase as determined from the quadratures  $I$  and  $Q$  of the cavity amplitude, corresponding to coherent pulsed masing with bandwidths ranging from around 120 kHz to 350 kHz. After the early sequence of discrete pulses, subsequent ones start to merge, transforming into a quasi-continuous and sustained cavity emission that persists for more than 500  $\mu s$ .

In Fig. 2, we focus on the spectral characteristics of the quasi-continuous masing emission. The extended cavity dynamics, shown in Fig. 2a, is measured with the same system parameters as in Fig. 1c but at half the digitizer sample rate in the heterodyne detection chain. The recorded quadratures  $I$  and  $Q$  of the cavity amplitude are demodulated at an intermediate frequency of 5 MHz detuned from the cavity resonance. We extract the emission's linewidth by employing fast Fourier transform (FFT) analysis and Lorentzian profile fitting within the integration window of 200  $\mu s$  (see Fig. 2b). Shifting the start of the integration window  $t_F$ , we analyze in Fig. 2c how the central frequency of the masing

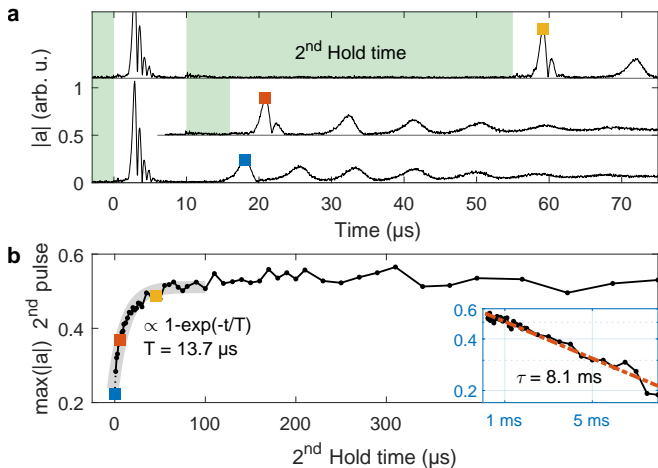


FIG. 3. **Influence of second hold time on revival dynamics.** **a**, Stacked cavity signals of the superradiant dynamics with a second stabilization sequence (hold time), represented by light green shading. Increasing the duration of this second hold time extends the spectral hole-filling process, influencing the amplitude of the superradiant masing pulse revival. **b**, Revival amplitude for varying second hold times, showing a sharp initial increase, and an exponential decrease for very long timescales.

emission drifts over time within  $\pm 25$  kHz. The observed linewidth, varying from 5 kHz to 20 kHz, is two orders of magnitude below the cavity linewidth  $\kappa$  and the individual spin linewidth  $\gamma_{\perp}$ , highlighting the crucial role of collective enhancement – an indicative trait of superradiance – in achieving high coherence. We attribute the linewidth variation to the emission frequency drift within the integration window, likely caused by magnetic field fluctuations. These fluctuations are three orders of magnitude smaller than the full magnetic field created by the detuning loop.

To investigate the cause of the unexpected revival pulses and quasi-continuous masing, we conducted a set of auxiliary measurements. Rapidly detuning the spins right after the initial superradiant decay inhibits the spin system’s interaction with the cavity mode, effectively introducing a second hold time. Extending this second hold time leads to an increase in the amplitude of the first superradiant pulse afterward, see Fig. 3a. The amplitude increase has a characteristic timescale of  $T = 13.7$   $\mu$ s, as shown in Fig. 3b. This result suggests that the cavity plays no role in the mechanism driving the pulsed revivals. They persist even when the spins are off-resonant with the cavity. Over time, this mechanism leads to an increase in spin inversion, which gets converted into cavity photons upon release of the superradiant decay. The amplitude decrease over very long times has been discussed previously in Ref. [19].

### Effective model

To gain deeper insights into the underlying dynamical

processes, we take a closer look at the semi-classical model. In our simulations, we discretize the spin frequency distribution into a number  $N_{\rho} = 501$  of numerical spin packets with index  $j$  and different weights  $\rho_j$ , as plotted in Fig. 4a. For simulating the initial superradiant decay, we initialize all spins with uniform inversion  $p_0$  and a small non-zero  $\langle \sigma_{-}^j \rangle$  component, to account for the triggering of the superradiant decay. We adjust only the value of  $p_0$  and a time offset to simulate the measured signals as in Fig. 1b. The simulation illustrates that during the superradiant decay, only spins close to the cavity resonance are selectively de-excited, creating a spectral hole in the spin distribution, as shown in Fig. 4a for  $t = 7$   $\mu$ s (red mark in Fig. 4b). After the superradiant decay has occurred, the instability threshold, now evaluated by summing over the product of each spin packet’s weighted inversion and cooperativity, represented graphically in Fig. 4a, and denoted as  $\overline{pC} = \sum_j \rho_j N_{\rho} \langle \sigma_z^j \rangle C_j$ , drops below 1. This indicates stabilization of the ensemble, preventing superradiant emission at later times.

To model the pulsed revivals while leaving the initial superradiant decay virtually unaffected, we introduce a new term to the Maxwell-Bloch equations that induces a gradual filling of the spectral hole. This additional term allows each spin packet  $j$  to slowly approach the mean ensemble inversion  $p = \sum_k \rho_k \langle \sigma_z^k \rangle$  with a characteristic relaxation rate  $\mathcal{J}$ , expressed as

$$\frac{d}{dt} \langle \sigma_z^j \rangle = \Lambda_{\langle \sigma_z^j \rangle} + \mathcal{J} (p - \langle \sigma_z^j \rangle), \quad (1)$$

where  $\Lambda_{\langle \sigma_z^j \rangle}$  stands for the coherent (relaxation-free) part of the dynamics of the system (see Supplementary Methods). We also include a small constant drive  $\eta$ , steadily contributing to the right-hand side of  $\frac{d}{dt} \langle a \rangle$ , modeling the effect of cavity noise and intrinsic fluctuations that continually trigger the recurring superradiant emission pulses. These intrinsic fluctuations are caused by quantum, thermal and technical noise effects and necessitate a higher-order cumulant expansion for a rigorous description [23]. To simplify the analysis we restrict ourselves to the first-order semi-classical description using  $\eta$  to effectively model these stochastic processes. In Fig. 4b we see the simulated effective filling of the spectral hole over time, where inversion is transferred inwards from the sides of the spin distribution. The corresponding simulated cavity amplitude captures qualitatively the measured dynamics, as shown in Fig. 4c. The value of the hole-filling rate  $\mathcal{J}/2\pi = 16$  kHz used in this simulation is in good agreement with the measured timescale  $T \sim \mathcal{J}^{-1}$  in Fig. 3b. Notably,  $\mathcal{J}$  is still on the same order of magnitude than the average nearest-neighbor spin-spin interaction strength  $J_n/2\pi \approx 52$  kHz.

The interplay of the gradual spectral hole-filling and the threshold behavior  $\overline{pC} > 1$  gives rise to the appearance of pulsed revivals, as plotted in Fig. 4c. The revival

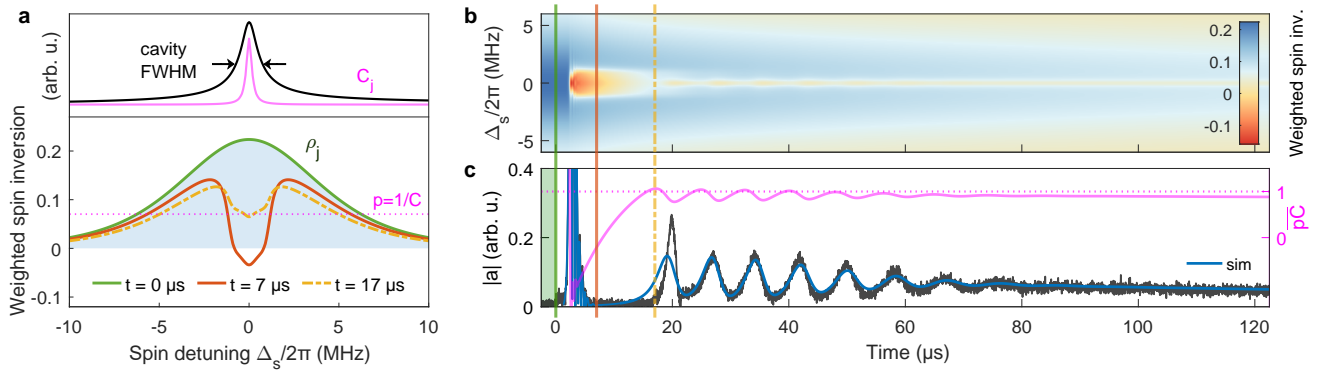


FIG. 4. **Simulation of superradiant dynamics with effective relaxation rate model.** **a**, Initial spin distribution showing a homogeneously inverted ensemble (green), a deep spectral hole after superradiant decay (red), a partially refilled hole before the first revival pulse (yellow). The y-axis scaling represents a weighted spin inversion  $\rho_j \langle \sigma_z^j \rangle$  of the center frequency bin. For comparison, we show the cavity resonance (black) together with the spin packet's cooperativities  $C_j$  (pink). **b**, Color plot illustrating the simulated spin inversion dynamics for spin packets with different detunings. Vertical lines indicate three crucial time steps highlighted in **a**. **c**, Measured and simulated cavity amplitude  $|a|$  using the spectral hole-filling model. We also plot the weighted instability threshold  $\overline{pC}$  over time.

pulses appear as soon as the threshold is exceeded and the inverted spin state becomes unstable again, being triggered by the noise photons in the cavity. Each revival pulse extracts inversion, reducing the overall value of  $p$ , while individual spectral holes become shallower, requiring less time to fill. However, the consecutive pulses take longer to reach their maximum amplitude, as the self-accelerating superradiant avalanche process is slower when starting with a lower effective number of participating spins. Thus, the increasing delay time is inversely proportional to  $p$  [24]. As the threshold value  $\overline{pC}$  oscillates distinctly above and below 1 for initially separated superradiant pulses, oscillations decrease as the pulses merge. A quasi-steady state is eventually reached, where energy lost via the cavity is replenished by a steady in-streaming from the sides of the spin distribution, while the threshold remains below 1. The process halts when the masing emission cannot be upheld due to significant inversion loss.

We provide additional evidence supporting the spectral hole-filling model in Fig. 5 we show that deliberately creating a spectral hole with a microwave pulse during the preparation of the inverted state can closely replicate the dynamics when the hole is generated by the initial superradiant decay. Moreover in Fig. 6 we demonstrate that the spectral hole filling time  $\Delta t$  is consistently related to the effective area of the spectral hole given by  $p_0 \kappa$ . The depth of a spectral hole is correlated with the initial inversion  $p_0$ , as the spins involved in the superradiant decay effectively undergo a  $\pi$ -rotation. The width of a spectral hole is determined by the cavity linewidth  $\kappa$ , given that only spins within the cavity linewidth interact with the mode. The relation  $\Delta t \propto p_0 \kappa$  holds across various cooldowns with different cavity linewidths.

### Spin-spin interactions

Our results suggest that direct spin-spin interactions play a crucial role in the spectral hole-filling process. Spin-

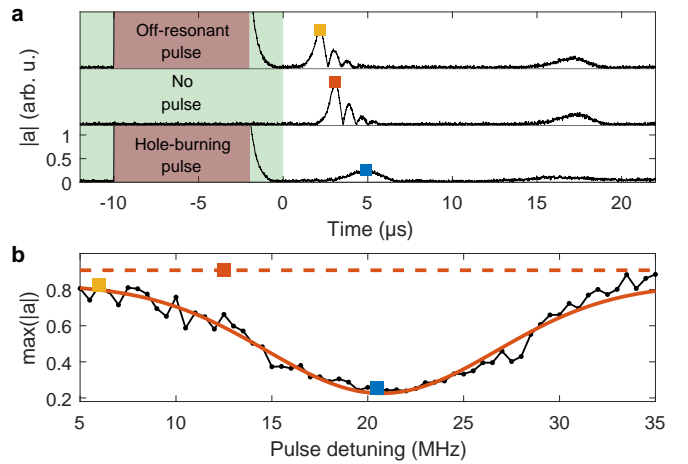


FIG. 5. **Probing superradiant dynamics after a hole-burning pulse.** **a**, Cavity dynamics when applying a strong microwave pulse (red shading) to the spins while detuned (green shading) and subsequently triggering the superradiant decay and revival pulses. This will create a spectral hole in the ensemble, resulting in a slice of decreased spin inversion at varying frequencies for different runs. A resonant hole-burning pulse reproduces a spectral hole similar to the one created by the initial superradiant decay when no hole-burning pulse is applied. When the hole-burning pulse is off-resonant at the sides of the spin distribution, it still leads to an earlier triggering of the initial superradiant decay, but will otherwise recreate similar dynamics as when no pulse is applied. **b**, Maximum amplitude of the superradiant decay pulse for different hole-burning frequencies, revealing the frequency distribution of the detuned spins, although appearing with a larger width due to power broadening.

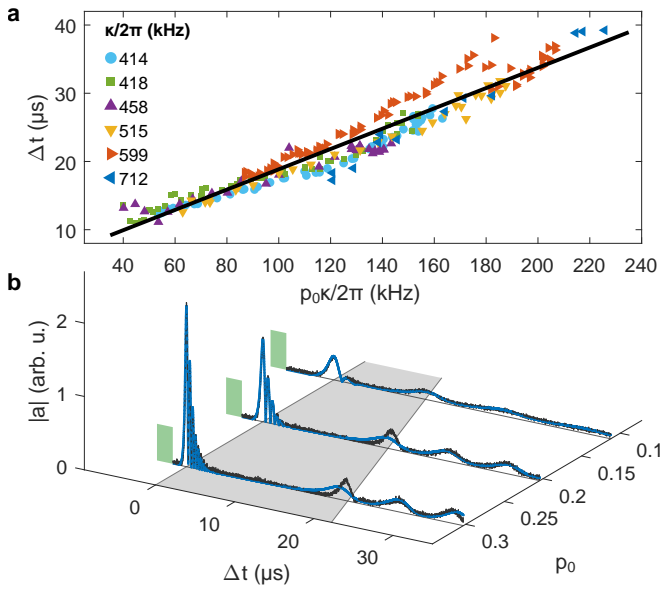


FIG. 6. **Influence of effective spectral hole area on the refilling time.** **a**, Evaluation of multiple cooldowns with different cavity linewidths  $\kappa$ , measuring revival dynamics. Notably, the change of linewidth is likely attributed to evaporation of the grease used to secure the diamond sample in place, resulting in a cleaner surface over several cooldown cycles. Our focus here lies on the effective area of the spectral hole generated by the initial superradiant decay, characterized by its depth and width. The depth of a spectral hole correlates with the initial inversion  $p_0$ , as the spins involved in the superradiant decay effectively undergo a  $\pi$ -rotation. Meanwhile, the width is determined by  $\kappa$ , given that only spins within the cavity linewidth interact with the mode. The initial inversion  $p_0$  is extracted from the initial superradiant decay using our numerical model, adjusting  $\kappa$  while keeping other model parameters constant. The time difference  $\Delta t$  of the maxima from the initial superradiant decay to the first revival pulse is compared with the effective area of the spectral hole  $p_0\kappa$ , showing a consistent linear trend. This time difference is a measure of the duration required to fill up the spectral hole with effective area  $p_0\kappa$ , bringing the ensemble above the threshold for  $\overline{pC}$  to allow for the superradiant revival pulse. **b**, Three experimental runs with different initial inversions  $p_0$  for the cooldown with  $\kappa/2\pi = 418$  kHz, illustrating the methodology to attain  $\Delta t$ .

phonon processes cannot provide the necessary mechanism, as they are too weak with a long spin-lattice relaxation time of  $T_1 \approx 134$  s in our sample [19] and the phonon modes not being populated at 25 mK [25]. A simple dynamics involving spin-flips between neighboring spins is insufficient to explain the observed behavior. A network of resonant single spins is characterized by comparable energy mismatches determined from the difference of individual spin detunings  $|\Delta_s^i - \Delta_s^j| \sim W$  and coupling rates  $J_{ij}$ . It remains disconnected because the number of resonant single spins  $nVJ_{ij}/W$  in a sample with density  $n$  stays constant as the volume  $V$  grows, with the dipole-dipole interaction scaling as  $J_{ij} \propto r^{-3}$ .

The interconnection within the spin network only appears when higher-order many-body interactions are considered, leading to a divergence in the number of resonant spin *pairs* with growing volume. The lowest-order relevant process involves the dynamics between different spin pairs, satisfying energy conservation in a four-spin resonance condition. These dynamics enable percolation in spin-excitation transport by connecting resonant spin pairs into an extended network, as demonstrated in Ref. [26]. This network connects spins not only in space but also on different energies, thus providing a many-body mechanism for refilling of the spectral hole.

## Discussion

Our experimental platform provides a new path toward fundamental insights into higher-order many-body interactions within disordered spin systems, unraveling the impact of long-range interactions on the relaxation processes of quantum many-body systems. The observed spectral hole refilling requires that a *typical eigenstate* [27] in the interacting spin network – when projected onto the basis-states of non-interacting spins – has a spectral bandwidth that is broader than the width of the spectral hole. This allows for the transfer of spin excitations from the spins outside into the spectral hole and hence for equilibration over time. This may shed some new light on eigenstate thermalization and the associated dynamics [28, 29] in closed and open many-body systems. Beyond these fundamental aspects, our work holds implications for advancing quantum technologies, particularly in spin-based microwave amplification [30] and solid-state masers [31], with expected ultranarrow linewidths [32].

## Acknowledgments

We thank E. Demler, H. Ritsch, S. Yelin, and T. Zhang for fruitful discussions. We acknowledge support by the Austrian Science Fund (FWF) projects I3765 (MICROSENS), P34314 (Spins in Quantum Solids). W.J.M and K.N would like to acknowledge support from the MEXT Quantum Leap Flagship Program (MEXT QLEAP) Grant No. JPMXS0118069605.

\* [wenzelkersten@gmail.com](mailto:wenzelkersten@gmail.com)

† [schmiedmayer@atomchip.org](mailto:schmiedmayer@atomchip.org)

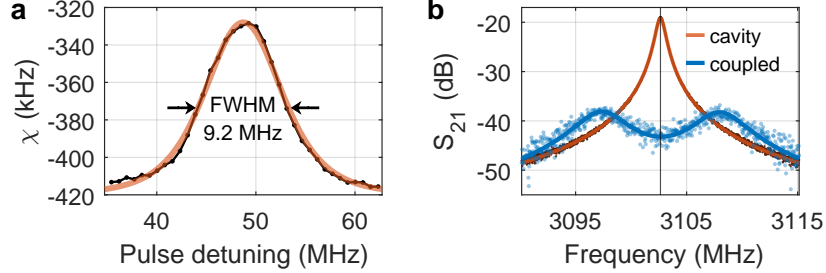
- [1] H. Walther, B. T. Varcoe, B.-G. Englert, and T. Becker, Cavity quantum electrodynamics, *Reports on Progress in Physics* **69**, 1325 (2006).
- [2] R. H. Dicke, Coherence in spontaneous radiation processes, *Physical Review* **93**, 99 (1954).
- [3] M. O. Scully and A. A. Svidzinsky, The super of superradiance, *Science* **325**, 1510 (2009).
- [4] M. Gross and S. Haroche, Superradiance: An essay on the theory of collective spontaneous emission, *Physics Reports* **93**, 301 (1982).
- [5] W.-K. Mok, A. Asenjo-Garcia, T. C. Sum, and L.-C.

- Kwek, Dicke superradiance requires interactions beyond nearest neighbors, *Physical Review Letters* **130**, 213605 (2023).
- [6] K. Hepp and E. H. Lieb, On the superradiant phase transition for molecules in a quantized radiation field: the Dicke maser model, *Annals of Physics* **76**, 360 (1973).
- [7] Y. K. Wang and F. Hioe, Phase transition in the Dicke model of superradiance, *Physical Review A* **7**, 831 (1973).
- [8] K. Baumann, C. Guerlin, F. Brennecke, and T. Esslinger, Dicke quantum phase transition with a superfluid gas in an optical cavity, *Nature* **464**, 1301 (2010).
- [9] G. Ferioli, A. Glicenstein, I. Ferrier-Barbut, and A. Browaeys, A non-equilibrium superradiant phase transition in free space, *Nature Physics* **19**, 1345 (2023).
- [10] A. F. van Loo, A. Fedorov, K. Lalumière, B. C. Sanders, A. Blais, and A. Wallraff, Photon-mediated interactions between distant artificial atoms, *Science* **342**, 1494 (2013).
- [11] M. O. Araújo, I. Krešić, R. Kaiser, and W. Guerin, Superradiance in a large and dilute cloud of cold atoms in the linear-optics regime, *Physical Review Letters* **117**, 073002 (2016).
- [12] T. Zhong, J. M. Kindem, J. Rochman, and A. Faraon, Interfacing broadband photonic qubits to on-chip cavity-protected rare-earth ensembles, *Nature Communications* **8**, 14107 (2017).
- [13] J. Kim, D. Yang, S.-h. Oh, and K. An, Coherent single-atom superradiance, *Science* **359**, 662 (2018).
- [14] G. Rainò, M. A. Becker, M. I. Bodnarchuk, R. F. Mahrt, M. V. Kovalenko, and T. Stöferle, Superfluorescence from lead halide perovskite quantum dot superlattices, *Nature* **563**, 671 (2018).
- [15] M. Scheibner, T. Schmidt, L. Worschech, A. Forchel, G. Bacher, T. Passow, and D. Hommel, Superradiance of quantum dots, *Nature Physics* **3**, 106 (2007).
- [16] C. Zhu, S. C. Boehme, L. G. Feld, A. Moskalenko, D. N. Dirin, R. F. Mahrt, T. Stöferle, M. I. Bodnarchuk, A. L. Efros, P. C. Sercel, et al., Single-photon superradiance in individual caesium lead halide quantum dots, *Nature*, 1476 (2024).
- [17] C. Bradac, M. T. Johnsson, M. v. Breugel, B. Q. Baragiola, R. Martin, M. L. Juan, G. K. Brennen, and T. Volz, Room-temperature spontaneous superradiance from single diamond nanocrystals, *Nature Communications* **8**, 1205 (2017).
- [18] A. Angerer, K. Streltsov, T. Astner, S. Putz, H. Sumiya, S. Onoda, J. Isoya, W. J. Munro, K. Nemoto, J. Schmiedmayer, et al., Superradiant emission from colour centres in diamond, *Nature Physics* **14**, 1168 (2018).
- [19] W. Kersten, N. de Zordo, O. Diekmann, T. Reiter, M. Zens, A. N. Kanagin, S. Rotter, J. Schmiedmayer, and A. Angerer, Triggered superradiance and spin inversion storage in a hybrid quantum system, *Physical Review Letters* **131**, 043601 (2023).
- [20] B. Julsgaard and K. Mølmer, Dynamical evolution of an inverted spin ensemble in a cavity: Inhomogeneous broadening as a stabilizing mechanism, *Physical Review A* **86**, 063810 (2012).
- [21] N. Skribanowitz, I. P. Herman, J. C. MacGillivray, and M. S. Feld, Observation of Dicke superradiance in optically pumped HF gas, *Physical Review Letters* **30**, 309 (1973).
- [22] H. J. Carmichael, Statistical methods in quantum optics 1: master equations and Fokker-Planck equations, Vol. 1 Springer Science & Business Media, (1999).
- [23] R. Kubo, Generalized cumulant expansion method, *Journal of the Physical Society of Japan* **17**, 1100 (1962).
- [24] L. Moi, P. Goy, M. Gross, J. M. Raimond, C. Fabre, and S. Haroche, Rydberg-atom masers. I. A theoretical and experimental study of super-radiant systems in the millimeter-wave domain, *Physical Review A* **27**, 2043 (1983).
- [25] T. Astner, J. Gugler, A. Angerer, S. Wald, S. Putz, N. J. Mauser, M. Trupke, H. Sumiya, S. Onoda, J. Isoya, et al., Solid-state electron spin lifetime limited by phononic vacuum modes, *Nature Materials* **17**, 313 (2018).
- [26] N. Y. Yao, C. R. Laumann, S. Gopalakrishnan, M. Knap, M. Mueller, E. A. Demler, and M. D. Lukin, Many-body localization in dipolar systems, *Physical Review Letters* **113**, 243002 (2014).
- [27] S. Goldstein, J. L. Lebowitz, C. Mastrodonato, R. Tumulka, and N. Zanghi, Normal typicality and von Neumann's quantum ergodic theorem, *Proceedings of the Royal Society A: Mathematical, Physical and Engineering Sciences* **466**, 3203 (2010).
- [28] M. Srednicki, Chaos and quantum thermalization, *Phys. Rev. E* **50**, 888 (1994).
- [29] M. Srednicki, The approach to thermal equilibrium in quantized chaotic systems, *Journal of Physics A: Mathematical and General* **32**, 1163 (1999).
- [30] A. Sherman, O. Zgadzai, B. Koren, I. Peretz, E. Laster, and A. Blank, Diamond-based microwave quantum amplifier, *Science Advances* **8**, eade6527 (2022).
- [31] J. D. Breeze, E. Salvadori, J. Sathian, N. M. Alford, and C. W. Kay, Continuous-wave room-temperature diamond maser, *Nature* **555**, 493 (2018).
- [32] Q. Wu, Y. Zhang, X. Yang, S.-L. Su, C. Shan, and K. Mølmer, A superradiant maser with nitrogen-vacancy center spins, *Science China Physics, Mechanics & Astronomy* **65**, 1 (2022).
- [33] K. Sandner, H. Ritsch, R. Amsüss, C. Koller, T. Nöbauer, S. Putz, J. Schmiedmayer, and J. Majer, Strong magnetic coupling of an inhomogeneous nitrogen-vacancy ensemble to a cavity, *Physical Review A* **85**, 053806 (2012).
- [34] M. Tavis and F. W. Cummings, Exact solution for an  $N$ -molecule—radiation-field Hamiltonian, *Physical Review* **170**, 379 (1968).

## Supplementary Material for: Self-Induced Superradiant Masing

### Spin ensemble

The spin system used in this work is the negatively charged nitrogen-vacancy center in diamond. The ground state Hamiltonian of the defect with spin  $S = 1$  is given by  $\mathcal{H} = \hbar D S_z^2 + \mu \vec{B} \cdot \vec{S}$ , with the zero field splitting  $D/2\pi = 2.88$  GHz and  $\mu/2\pi = 28$  MHz mT $^{-1}$ . The diamond is cut from a larger sample with an initial nitrogen concentration of approximately 200 ppm and naturally abundant  $^{13}\text{C}$  isotopes, treated with neutron irradiation with a total fluence of  $5 \times 10^{17}$  cm $^{-2}$  for 50 h for the creation of lattice vacancies, and subsequently annealed at 900 °C for 3 h for the formation of NV $^-$  centers. The high amount of lattice damage due to the neutron irradiation is the reason for the large inhomogeneous broadening  $W/2\pi = 9.2$  MHz and rather short  $T_2 = 1/\gamma_{\perp} \approx 0.9$   $\mu\text{s}$ .



Supplementary Fig. 1. **Spin distribution and steady-state spectroscopy measurements.** **a**, Measurement of the inhomogeneously broadened spin distribution in the dispersive regime, with spins detuned by around  $\delta/2\pi \approx 50$  MHz from the cavity. Following a 100 ms weak microwave drive at different frequencies, with the spin system initially in the ground state, only spins with the corresponding frequency will end up in an equal mixture of up and down spins, while other spins are unaffected. This change in the overall spin ensemble inversion leads to a dispersive shift  $\chi \propto \langle S_z \rangle$  of the cavity resonance frequency, measured using a vector network analyzer. **b**, Transmission spectroscopy of the cavity using high (red) and low (blue) microwave power. Using high input power, the whole spin ensemble is brought into a completely mixed state, effectively decoupling it from the cavity. A Lorentzian fit yields a linewidth of  $\kappa/2\pi = 418$  kHz. Using low input power, the normal-mode splitting of the coupled system in the ground state is measured and fitted with a collective coupling strength of  $g_{\text{coll}}/2\pi = 4.6$  MHz.

### Hybrid system characterization

We measure the inhomogeneously broadened spin distribution in the dispersive regime, as shown in Supplementary Fig. 1a. This distribution is well described by a  $q$ -Gaussian function [33]

$$\rho(\omega) = (1 - (1 - q)(\omega - \omega_0)^2/\delta_q^2)^{\frac{1}{1-q}}, \quad (2)$$

with  $\delta_q = W\sqrt{(q-1)/(2^{q-1}-1)}$ , where  $W$  is the full-width at half-maximum, using a value for the shape parameter of  $q = 1.39$ . We determine the cavity linewidth  $\kappa/2\pi = 418$  kHz, by measuring the steady-state transmission of the coupled system with a high input power of the vector network analyzer, see Supplementary Fig. 1b. This brings the whole spin ensemble into a completely mixed state, effectively decoupling it from the cavity. Using low input power, we measure the normal-mode splitting of the system in the ground state. A steady-state solution of Eqs. (4) provides the fitted value of  $g_{\text{coll}}/2\pi = 4.6$  MHz. Comparing this value with the single spin coupling  $g_0/2\pi \approx 2$  Hz (obtained from a finite-element simulation of the cavity) we get an estimation of the number of spins  $N = g_{\text{coll}}^2/g_0^2 \approx 5.3 \times 10^{12}$ . Taking the volume of the diamond sample of around  $5.1 \times 10^6$   $\mu\text{m}^3$  and the carbon density in diamond of  $n_c = 1.755 \times 10^{23}$  cm $^{-3}$  into account results in an NV $^-$  concentration of approximately 6 ppm.

### Microwave setup, cavity, and inversion pulse

We employ I/Q mixing with an arbitrary waveform generator and a microwave source at the cavity frequency to synthesize the inversion pulse. After amplification with a high-power amplifier, the pulse is injected into cavity port 1.

The outgoing signal, exiting at cavity port 2, undergoes further amplification both inside and outside the cryostat. It is demodulated using another frequency source and recorded by a digitizer with a maximum sampling rate of 2 GHz. Additional details on the superconducting cavity design and the protocol for initializing the inverted state, including details of the inversion pulse and detuning loop switching, can be found in Ref. [19].

### Effective theory

Our system is described by the driven Tavis-Cummings Hamiltonian in the rotating frame [34],

$$\mathcal{H} = \hbar \Delta_c a^\dagger a + \frac{\hbar}{2} \sum_i \Delta_s^i \sigma_z^i + i \hbar g_0 \sum_i (a^\dagger \sigma_-^i - \sigma_+^i a) + i \hbar \eta (a^\dagger - a), \quad (3)$$

with  $a^\dagger(a)$  being the creation (annihilation) operator of the cavity mode and  $\sigma_z^i, \sigma_\pm^i$  being the Pauli- $z$  and raising/lowering operators for the  $i^{\text{th}}$  spin, respectively. A possible external driving field is represented by  $\eta$ . In our simulations, we discretize the spin frequency distribution  $\rho(\omega)$  into  $N_\rho = 501$  spin packets with equal spacing. Each of the  $N_\rho$  numerical spins, indexed by  $j$ , couples to the cavity with coupling strength  $g_\rho = g_{\text{coll}}/\sqrt{N_\rho}$  and is weighted according to  $\sum_j \rho_j = 1$ . The inhomogeneous broadening of the spin ensemble is modeled with the detunings  $\Delta_s^j = \omega_s^j - \omega_p$ , while  $\Delta_c = \omega_c - \omega_p$  describes the detuning of the cavity, both with respect to the driving frequency  $\omega_p$ .

The system's losses caused by coupling to the environment are accounted for by introducing a cavity loss rate  $\kappa$  and a spin decoherence rate  $\gamma_\perp$  using a Lindblad master equation approach. We disregard  $T_1$  processes as the spin-lattice relaxation rate is negligible compared to all other dynamical timescales of our system. To simplify the analysis, higher-order correlations between spins and cavity are neglected, ending up with the well-known Maxwell-Bloch equations,

$$\frac{d}{dt} \langle a \rangle = -(\kappa + i \Delta_c) \langle a \rangle + g_\rho N_\rho \sum_j \rho_j \langle \sigma_-^j \rangle + \eta, \quad (4a)$$

$$\frac{d}{dt} \langle \sigma_-^j \rangle = -(\gamma_\perp + i \Delta_s^j) \langle \sigma_-^j \rangle + g_\rho \langle a \rangle \langle \sigma_z^j \rangle, \quad (4b)$$

$$\frac{d}{dt} \langle \sigma_z^j \rangle = -2g_\rho \left( \langle a^\dagger \rangle \langle \sigma_-^j \rangle + \langle a \rangle \langle \sigma_+^j \rangle \right) + \mathcal{J} (p - \langle \sigma_z^j \rangle). \quad (4c)$$

The last term in Eq. (4c) phenomenologically describes the gradual filling of a spectral hole at the relaxation rate  $\mathcal{J}$  up to the mean ensemble inversion  $p = \sum_k \rho_k \langle \sigma_z^k \rangle$ , cf. Eq. (1). We solve these equations numerically to qualitatively model the observed superradiant masing phenomena.

The instability criterion  $\overline{pC} > 1$  and the effective ensemble linewidth  $\Gamma$  are evaluated using the following definition

$$C = \sum_j \rho_j N_\rho C_j = \frac{g_\rho^2 N_\rho}{\kappa} \sum_j \rho_j \left( \gamma_\perp + \frac{\Delta_s^j}{\gamma_\perp} \right)^{-1} = \frac{g_{\text{coll}}^2}{\kappa \Gamma}. \quad (5)$$

### Spin-spin interaction

We evaluate the nearest-neighbor dipole coupling rate  $J_n$  from the prefactor in the Hamiltonian

$$\mathcal{H}_{\text{dipole}} = -\hbar \sum_{i,j>i} \underbrace{\frac{\mu_0 \mu^2 \hbar}{4\pi r_{ij}^3}}_{J_{ij}} [3(\mathbf{S}_i \cdot \hat{\mathbf{r}}_{ij})(\mathbf{S}_j \cdot \hat{\mathbf{r}}_{ij}) - \mathbf{S}_i \cdot \mathbf{S}_j] \quad (6)$$

using the typical distance between  $\text{NV}^-$  spins of  $r = n^{-1/3} \approx 10$  nm, where  $n$  is the density of  $\text{NV}^-$  spins with 6 ppm in the diamond lattice. This results in a value for the typical strength of the nearest-neighbor coupling rate of  $J_n/2\pi \approx 52$  kHz.